

Extremely short-length surface plasmon resonance sensors

Maxim L. Nesterov^{1*}, Alexandre V. Kats¹ and Sergei K. Turitsyn²

¹*A. Ya. Usikov Institute for Radiophysics and Electronics NAS of Ukraine,
12 Academician Proskura Street, 61085 Kharkov, Ukraine.*

²*Photonics Research Group, School of Engineering and Applied Science, Aston University,
Birmingham B4 7ET, United Kingdom.*

*Corresponding author:
nesterovml@gmail.com

Abstract: The impact of the system design on the control of coupling between planar waveguide modes and surface plasmon polaritons (SPP) is analyzed. We examine how the efficiency of the coupling can be enhanced by an appropriate dimensioning of a multi-layer device structure without using additional gratings. We demonstrate that by proper design the length of the device can be dramatically reduced through fabrication a surface plasmon resonance sensor based on the SPP-photon transformation rather than on SPP dissipation.

© 2021 Optical Society of America

OCIS codes: (240.6680) Surface plasmons; (060.2370) Fiber optics sensors

References and links

1. H. Raether, *Surface Plasmons* (Springer-Verlag, New York, 1988).
2. V. M. Agranovich and D. L. Mills, *Surface Polaritons*, (Nauka, Moscow, 1985).
3. A.V. Zayats and I.I. Smolyaninov, "Near-field photonics: surface plasmons polaritons and localized surface plasmons," *J. Opt. A: Pure Appl. Opt.* **5**, S16-S50 (2003).
4. A. V. Zayats, I. I. Smolyaninov, and A. A. Maradudin, "Nano-optics of surface plasmon polaritons," *Phys. Rep.* **408**, 131 (2005).
5. S.I. Bozhevolnyi and V.M. Shalaev, "Nanophotonics with Surface Plasmons," *Photonics Spectra*, Part I, 58; Part II, 68 (2006).
6. M. I. Stockman, "Electromagnetic Theory of SERS," in *Springer Series Topics in Applied Physics*, edited by K. Kneipp, M. Moskovits and H. Kneipp, *Surface Enhanced Raman Scattering Physics and Applications* (Springer-Verlag, Heidelberg New York Tokyo, 2006).
7. Jiri Homola, Sinclair S. Yee, and Gunter Gauglitz, "Surface plasmon resonance sensors: review," *Sens. Actuators, B* **54**, 3-15 (1999).
8. J. Homola, "Present and future of surface plasmon resonance biosensors (review)," *Anal. Bioanal. Chem.* **377**, 528-539 (2003).
9. P. V. Lambeck, "Integrated optical sensors for the chemical domain," *Meas. Sci. Technol.* **17**, R93-R116 (2006).
10. R.D. Harris, B.J. Luff, J.S. Wilkinson, J. Piehler, A. Brecht, G. Gauglitz, R.A. Abuknesha, "Integrated optical surface plasmon resonance immunoprobe for simazine detection," *Biosensors and Bioelectronics* **14**, 377-386 (1999).
11. R.D. Harris, J.S. Wilkinson, "Waveguide surface plasmon resonance sensors," *Sensors and Actuators B* **29**, 261-267 (1995).
12. H. J. M. Kreuzel, P. V. Lambeck, J. M. N. Beltman and T. J. A. Popma (1987) "Modecoupling in multilayer structures applied to a chemical sensor and a wavelength selective directional coupler," *Proc. ECIO'87* (Glasgow, 11-13 May) pp. 217-220.
13. V. Mikhailov, G. Wurtz, J. Elliott, P. Bayvel and A. V. P. Zayats, "Dispersing Light with Surface Plasmon Polaritonic Crystals," *Phys. Rev. Lett.* **99**, 083901-1 (2007).
14. A. V. Kats, M. L. Nesterov, and A. Yu. Nikitin, "Polarization properties of a periodically-modulated metal film in regions of anomalous optical transparency," *Phys. Rev. B.* **72**, 193405 (2005).

15. A. V. Kats, M. L. Nesterov, and A. Yu. Nikitin, "Excitation of surface plasmon-polaritons in metal films with double periodic modulation: Anomalous optical effects," *Phys. Rev. B* **76**, 045413 (2007).
16. S. I. Bozhevolnyi, J. E., K. Leosson, P. M. W. Skovgaard, and J. M. Hvam, "Waveguiding in Surface Plasmon Polariton Band Gap Structures," *Phys. Rev. Lett.* **86**, 3008 - 3011 (2001).
17. A. Boltasseva, T. Nikolajsen, K. Leosson, K. Kjaer, M. S. Larsen, and S. I. Bozhevolnyi, "Integrated optical components utilizing long-range surface plasmon polaritons," *Journal of Lightwave Technology*, **23**, 413-422 (2005)
18. S. I. Bozhevolnyi, V. S. Volkov, E. Devaux, J.-Y. Laluet and T. W. Ebbesen, "Channel plasmon subwavelength waveguide components including interferometers and ring resonators," *Nature* **440**, 508-511 (2006).
19. F. Lopez-Tejiera, S. G. Rodrigo, L. Martín-Moreno, F. J. García-Vidal, E. Devaux, T. W. Ebbesen, J. R. Krenn, I. P. Radko, S. I. Bozhevolnyi, M. U. Gonzalez, J.-C. Weeber and A. Dereux, "Efficient unidirectional nanoslit couplers for surface plasmons," *Nat. Phys.* **3**, 324-328 (2007).
20. G. Stewart et al., "Surface plasmon resonances in thin metal films for optical fiber devices," in *Proc. Optical Fiber Sensors*, Washington, DC, 1988, pp. 328-331.
21. W. Johnstone, G. Stewart, T. Hart, and B. Culshaw, "Surface plasmon polaritons in thin metal films and their role in fiber optic polarizing devices," *J. Lightwave Technol.* **8**, 538-44 (1990).
22. J. Homola and R. Slavik, "Fibre-Optic Sensor based on Surface Plasmon Resonance," *Electronics Letters* **32**, 480 (1996).
23. B. Gauvreau, A. Hassani, M. Fassi Fehri, A. Kabashin, and M. A. Skorobogatiy, "Photonic bandgap fiber-based Surface Plasmon Resonance sensors," *Opt. Express* **15**, 11413-11426 (2007)
24. G. Nemova, R. Kashyap, "Theoretical model of a planar integrated refractive index sensor based on surface plasmon-polariton excitation," *Opt. Commun.* **275**, 76-82, (2007).
25. Y. Y. Shevchenko and J. Albert, "Plasmon resonances in gold-coated tilted fiber Bragg gratings," *Opt. Lett.* **32**, 211-213 (2007)
26. M. Skorobogatiy and A. V. Kabashin, "Photon crystal waveguide-based surface plasmon resonance biosensor," *Appl. Phys. Lett.* **89**, 143518 (2006).
27. H. Ditlbacher, N. Galler, D.M. Koller, A. Hohenau, A. Leitner, F.R. Aussenegg and J.R. Krenn "Coupling dielectric waveguide modes to surface plasmon polaritons," *Opt. Express* **16**, 10455-10464 (2008).
28. T. Nakano, K. Baba, and M. Miyagi, "Insertion loss and extinction ratio of a surface plasmon-polariton polarizer: theoretical analysis," *J. Opt. Soc. Am. B* **11**, 2030-2035 (1994)
29. C-H Chen, L. Wang, "Design of Finite-length metal-clad optical waveguide polarizer," *IEEE J. Quantum Electron.* **34**, 1089-97 (1998).
30. S. G. Rodrigo, F. J. García-Vidal, and L. Martín-Moreno, "Influence of material properties on extraordinary optical transmission through hole arrays," *Phys. Rev. B* **77**, 075401 (2008).
31. E. D. Palik, *Handbook of Optical Constants and Solids*, (Academic, Orlando, 1985).
32. M.A. Ordal, L.L. Long, R.J. Bell, S. E. Bell, R. R. Bell, R.W. Alexander, and C. A. Ward, "Optical properties of the metals Al, Co, Cu, Au, Fe, Pb, Ni, Pd, Pt, Ag, Ti, and W in the infrared and far infrared," *App. Opt.* **22**, 1099 (1983).
33. Katsunari Okamoto, *Fundamentals of Optical Waveguides* (Academic Press, first Edition, 2000).
34. Poche Yeh, *Optical Waves in Layered Media* (John Wiley & Sons, New York, 1988).
35. A. Yariv, *Quantum Electronics* (John Wiley & Sons, New York, 1975).
36. J. Ctyroky, J. Homola, P.V. Lambeck, S. Musa, H.J.W.M. Hoekstra, R.D. Harris, J.S. Wilkinson, B. Usievich, N.M. Lyndin, "Theory and modelling of optical waveguide sensors utilising surface plasmon resonance," *Sensors and Actuators B* **54** 66-73 (1999).
37. Yogendra S. Dwivedi, Anuj K. Sharma, B. D. Gupta, "Influence of Design Parameters on the Performance of a Surface Plasmon Resonance Based Fiber Optic Sensor," *Plasmonics* **3** 79-86 (2008).

1. Introduction

Recent advances in the application of surface plasmon polaritons in the fields of chemical and bio-sensors and nano-science has stimulated booming research and development. Surface plasmon resonance (SPR) based optical bio-sensors exploit a special type of the electromagnetic surface waves coupled to the collective electron excitation — surface plasmon polaritons (see e.g. [1–6]) to probe interactions between an analyte under study and a bio-molecular recognition element immobilized on the SPR sensor surface. One of the most important characteristics of the SPPs is their ability to detect small scale effects and field interactions at the interfaces between a metal and a non-metal. The surface plasmon polaritons attract a great deal of attention as a quite unique possibility of the electromagnetic field localization and corresponding substantial enhancement of the electric field near the surface. Such a high level of a field lo-

calization results into the enhanced sensitivity of the SPR sensors. Specifically, SPPs in sandwiched structures have attracted much interest as a promising way to implement surface plasmon resonance optical sensors [7–11]; waveguide-coupled SPR sensor was first demonstrated by Harrie Kreuwel in [12]. Many of the key properties of such sensors, using multi-layer sandwiched structures, are determined by the interaction between a waveguide and SPP modes. The progress in the area is very fast and some products are already commercially available. There is broad range of possible schemes and configurations, and despite successful first demonstrations of such devices, many design problems are still open and in this paper we examine some of these issues.

We would like to point out that SPP-based technology has a very broad spectrum of potential applications. A feasibility of exploiting the high spectral dispersion achievable in plasmonic devices in optical communication has been recently discussed in [13]. Surface waves play an important role in many fundamental resonant phenomena, such as e.g. the "Wood anomalies" in the reflectivity and transmissivity [1, 14, 15] of periodically corrugated metal samples, and are already practically exploited in a wide range of practical devices. A very important area of the SPP applications is in miniaturization and integration of optical circuits. A possibility of high localization of electromagnetic fields using SPP and subwavelength metal structures makes it possible to overcome the diffraction limit of light waves which is a critical issue in the development of photonic circuits. Considerable efforts have been recently placed into the development of plasmon subwavelength guiding and coupling devices [16–19].

A promising direction in the development of SPP-based devices and techniques is to combine surface plasmon approaches with well developed dielectric waveguide technologies, in particular with fiber-optics [20–23]. The conventional modern SPR fiber sensors utilize Bragg gratings or long period gratings to couple light to the SPPs. Recently the coupling efficiency between the core mode of the waveguide and SPP modes of the metal film in planar and cylindrical geometry for sensing purposes have been examined in [24–27]. A variety of possible configurations of multi-layered structures offers a range of potential device designs and this field is still far from been fully explored. Efficiency of the coupling between SPP modes and the waveguide is the key to unlocking the full potential of such sandwiched multi-layer structured devices. In this work we analyze the basic properties of the SPP and waveguide mode coupling and consider a possibility to optimize the SPR-sensors by system design through tuning device parameters rather than through additional gratings written in the waveguide. Understanding of the details of the interaction of the SPP and waveguide modes is a critical point in the development of the high sensitivity real-time SPR-sensor and our goal here is to analyze such interaction for rather general configuration that can be relevant to many practical situations.

2. Fields representation and boundary conditions

Consider eigenmodes of the multilayer structure depicted in Fig. 1 that is typical for the SPP-based devices. The indices c , b , w , $-$ and $+$ in what follows relate to the corresponding layers as shown in Fig. 1. Taking into account that SPP is a TM-polarized wave and, therefore, in the geometry under consideration it can interact only with TM-polarized waves, we consider TM-polarized eigenmodes ($\mathbf{E} = \{E_x, 0, E_z\}$, $\mathbf{H} = \{0, H, 0\}$) of the structure. The time dependence is moved out of the equations by the corresponding Fourier transform and analysis of the plane waves having the form $\exp(-i\omega t)$. We are interested here in solutions that present outgoing or decaying waves both in the upper half-plane $z \leq 0$ ($\tau = -$), and in the region $z \geq L + \ell + d$ ($\tau = +$) for any given frequency ω and tangential component of the wavevector k_x ,

$$H^\tau(x, z) = H^\tau \exp\{ik_x x + i\tau k_z^\tau [z - \delta_{\tau,+}(d + \ell + L)]\}, \quad (1)$$

where $k = \omega/c$ is the vacuum wavenumber, $k_z^\tau = \sqrt{k^2 \epsilon_\tau - k_x^2}$, $\text{Im}(k_z^\tau), \text{Re}(k_z^\tau) \geq 0$. Similarly,

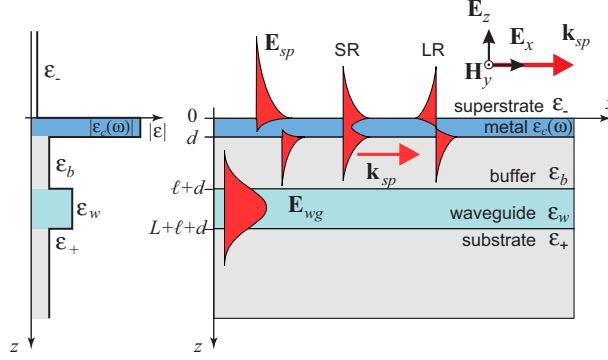


Fig. 1. Geometry of the problem and a typical dielectric permittivity distribution. The structure of the SPP modes for both thick and thin metal films are schematically shown along with a waveguide mode.

$$H^M(x, z) = \sum_{\sigma=\pm} H^{M|\sigma} \exp\{ik_x x + i\sigma k_z^M [z - z_M]\}, \quad (2)$$

in the metal ($M = c$, $z \in [0, d]$), the buffer ($M = b$, $z \in [d, d + \ell]$) and the waveguide ($M = w$, $z \in [d + \ell, d + \ell + L]$) layer. Here $z_c = 0$, $z_b = d$, $z_w = d + \ell$ and the branch of the square roots, k_z^M , is chosen so that $\text{Re}(k_z^M) \geq 0$, $\text{Im}(k_z^M) \geq 0$ and thus the sign $\sigma = +(-)$ corresponds to the waves propagating or decaying in the positive (negative) direction of the z -axis, respectively. The x -dependence in all the layers is the same due to conservation of the tangential momentum (or, equivalently, as imposed by the boundary conditions). The electric field components can be derived from the Maxwell equations. Assuming all the media shown in Fig. 1 to be non-magnetic we have

$$E_x^m(x, z) = -\frac{i}{k\epsilon_m} \frac{\partial}{\partial z} H^m(x, z), \quad (3)$$

$$E_z^m(x, z) = \frac{i}{k\epsilon_m} \frac{\partial}{\partial x} H^m(x, z), \quad (4)$$

where $m = \tau, c, b, w$, and ϵ_m denotes dielectric permittivity in the m -th layer (medium), and

$$E_u^\tau(x, z) = E_u^\tau \exp\{ik_x x + i\tau k_z^\tau [z - \delta_{\tau,+}(d + \ell + L)]\}, \quad (5)$$

$$E_u^M(x, z) = \sum_{\sigma=\pm} E_u^{M|\sigma} \exp\{ik_x x + i\sigma k_z^M [z - z_M]\}. \quad (6)$$

Here $u = x, y$ stays for the corresponding components of the electric field. The amplitudes of the electric field, E_u^τ , $E_u^{M|\sigma}$, can be expressed by means of Eqs. (3), (4) and (1), (2) as

$$E_x^\tau = \frac{\tau k_z^\tau}{k\epsilon_\tau} H^\tau, \quad E_z^\tau = -\frac{k_x}{k\epsilon_\tau} H^\tau, \quad (7)$$

$$E_x^{M|\sigma} = \frac{\sigma k_z^M}{k\epsilon_M} H^{M|\sigma}, \quad E_z^{M|\sigma} = -\frac{k_x}{k\epsilon_M} H^{M|\sigma}. \quad (8)$$

Introducing dimensionless variables,

$$\alpha = k_x/k, \quad \beta^m = \frac{k_z^m}{k\epsilon_m}, \quad (9)$$

Eqs. (7), (8) can be presented in the form

$$E_x^\tau = \tau \beta^\tau H^\tau, \quad E_z^\tau = -\frac{\alpha}{\epsilon_\tau} H^\tau, \quad (10)$$

$$E_x^{M|\sigma} = \sigma \beta^M H^{M|\sigma}, \quad E_z^{M|\sigma} = -\frac{\alpha}{\epsilon_M} H^{M|\sigma}. \quad (11)$$

Continuity of the tangential components of the field crossing the interfaces results in the system of eight linear homogeneous algebraic equations for the eight amplitudes of the magnetic field, $H^{M|\sigma}$, H^τ . The nontrivial solutions of these system (eigenmodes of the layered structure) exist when the determinant is equal to zero. This leads after straightforward algebra to the dispersion relation:

$$-\beta^w [ia^w \tan \phi - b^w] + \beta^+ [a^w - ib^w \tan \phi] = 0, \quad (12)$$

where

$$\begin{aligned} a^w &= a^b + b^b \tanh F, & b^w &= \frac{\beta^b}{\beta^w} [a^b \tanh F + b^b], \\ a^b &= 1 + \frac{\beta^-}{\xi} \tanh \Phi, & b^b &= \frac{\xi}{\beta^b} \left[\tanh \Phi + \frac{\beta^-}{\xi} \right], \end{aligned} \quad (13)$$

$\xi \equiv \beta^c$ is the surface impedance of the metal film, and

$$\Phi = -ik_z^c d, \quad \phi = k_z^w L, \quad F = -ik_z^b \ell. \quad (14)$$

Resolving Eq. (12) yields the dispersion curves, $\omega = \omega(k_x)$ [or $k_x = K(\omega)$] corresponding to different modes of the system. For the sake of clarity, but without loss of generality, in what follows we neglect frequency dependence of all dielectric permittivities except that one of the metal layer, $\epsilon_c = \epsilon_c(\omega)$. For the latter we will use the Drude model, $\epsilon_c(\omega) = \epsilon_\infty - \omega_p^2 / \omega(\omega + i\gamma)$, where ϵ_∞ is high-frequency value of the permittivity $\epsilon_c(\omega)$, ω_p is the plasma frequency, and γ is the damping rate. In Table 1 the typical parameters for the commonly used materials (for design of the sensors) are shown, here $n_m = \sqrt{\epsilon_m}$, $m = -, b, w, +$, denote refractive indices of the corresponding dielectric layers.

Table 1. Table of common material parameters for the SPR sensing devices*

metal	silver [7]	gold [7, 24, 25]	aluminium [28]
dielectric core	$n = 1.585$ [29]	$n = 1.476$ [28]	$n = 1.47$ [24]
dielectric cladding	$n = 1.439$ [29]	$n = 1.473$ [28]	$n = 1.45$ [24]

* For optical constants of silver, gold and aluminium see [30–32].

The field amplitudes can be expressed in terms of the upper medium magnetic field amplitude, H^- :

$$\begin{aligned} H^{c|\sigma} &= \frac{H^-}{2} \left(1 - \sigma \frac{\beta^-}{\beta^c} \right), & H^{b|\sigma} &= \frac{H^-}{2} \{ a^b - \sigma b^b \}, \\ H^{w|\sigma} &= \frac{H^-}{2} \{ a^w - \sigma b^w \}, & H^+ &= H^- [a^w \cos \phi - ib^w \sin \phi]. \end{aligned} \quad (15)$$

The dispersion relation includes a number of limiting cases corresponding to different combinations of thick or thin limits of the building layers. For instance, in the limit of a large

thickness of the buffer layer, $\ell \rightarrow \infty$ ($F \gg 1$), the dispersion relation splits into two dispersion branches,

$$\beta^b + \beta^+ - i \left(\beta^w + \frac{\beta^+ \beta^b}{\beta^w} \right) \tan \phi = 0, \quad (16)$$

$$a^b + b^b = 0, \quad (17)$$

which correspond to the waveguide TM modes and SPP modes of the metal film, respectively. In turn, the derived SPP dispersion relation, Eq. (17), for a rather thick metal film ($\Phi \gg 1$) limit leads to standard SPP modes, $a^b + b^b = 0 \Rightarrow (\beta^b + \xi)(\beta^- + \xi) = 0$. In the case of a finite value of Φ the dispersion relation describes the hybridized double-interface-localized SPP modes,

$$(\beta^b \tanh \Phi + \xi)(\beta^- \tanh \Phi + \xi) - \xi^2 \cosh^{-2} \Phi = 0. \quad (18)$$

More specifically, when the dielectric permittivities of the superstrate and the buffer coincide, $\varepsilon_b = \varepsilon_-$, then Eq. (18) splits into two branches and yields the dispersion relations for the short-range (symmetric) SPP and long-range (antisymmetric) SPP modes [1], see Fig. 1,

$$\beta^b = \beta_+^b \equiv -\xi \tanh(\Phi/2), \quad \beta^b = \beta_-^b \equiv -\xi \coth(\Phi/2), \quad (19)$$

where subscripts “+” and “-” correspond to the long-range (LR), and short-range (SR) mode, respectively.

Similar to that, the solitary waveguide modes ($\ell \rightarrow \infty$) depend on the waveguide layer thickness and permittivity. Namely, in this limiting case the solution of Eq. (16) reads

$$\varepsilon_w k L = \frac{1}{\beta^w} \arctan \left[-i \frac{(\beta^b + \beta^+) \beta^w}{(\beta^w)^2 + \beta^b \beta^+} \right] + \frac{n\pi}{\beta^w}, \quad n = 0, \pm 1, \dots \quad (20)$$

At the crossing points of the dispersion curves the phase matching conditions are satisfied and an interaction between waves of different branches is most efficient. However, in order to stress the difference between the situations when the phase matching conditions are provided by an additional grating and the problem considered here we will use in what follows term hybridization of modes. In the problem considered here the finite thickness of the buffer layer results in hybridization (combination) of the waveguide and SPP modes. The resulting hybrid eigenmodes of the system might have spatial distributions with energy both in the dielectric waveguide and in the SPP modes. We would like to emphasize that the most interesting situations for the design of the sensors takes place when the level of the mode hybridization (strong coupling of the waveguide and SPP modes) is rather high. This occurs when the buffer layer is relatively thin and in the vicinity of the points in the $\omega - k_x$ plane where the dispersion curves of the free SPP and waveguide modes intersect. In the vicinity of such points the hybridization is high and control of operation near this point can be provided by the adjustment of the buffer layer. This consideration outlines the design rules and explains the choice of the parameters in the examples presented below.

The solutions of the dispersion relation of the multi-layer system, Eq. (12), are plotted in Fig. 2 where we use the normalized frequency parameter $kL = L\omega/c$, versus the squared normalized tangential component of the wavenumber (i.e., the squared effective refraction index, $n_{\text{eff}}^2 \equiv \alpha^2 = c^2 k_x^2 / \omega^2$). The most interesting area for the parameters lies is the vicinity of the intersection between the silver-superstrate SPP branch and that of the lowest-frequency (fundamental) waveguide mode, see inset in Fig. 2.

The coupling of these modes due to the finite-thickness of the buffer layer results in a repulsion of the dispersion branches. However, in the vicinity of the inoculating curves intersection

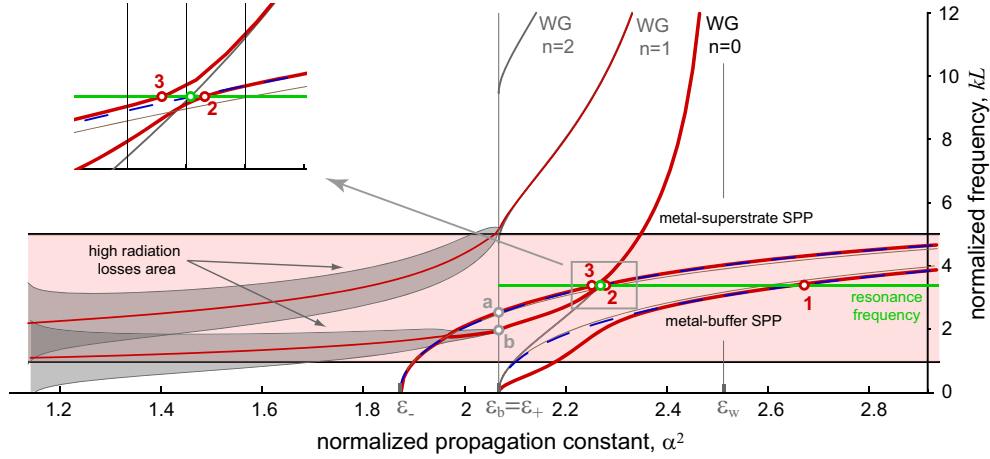


Fig. 2. Dispersion relations for the multi-layer system of Fig. 1. Thick (red) curves represent the solutions of the complete dispersion relation given in Eq. (12). Thin (gray) WG-named curves correspond to the dispersion relation of the solitary dielectric waveguide, Eq. (20), and a thick silver metal film, $d \rightarrow \infty$. The dashed (blue) curves represent the high-frequency and low-frequency solutions of the dispersion relation for a solitary thin silver metal film. The parameters are: $n_- = 1.37$, $n_b = n_+ = 1.439$, $n_w = 1.585$, the thicknesses of the layers are $d = 58$ nm, $\ell = 400$ nm, $L = 250$ nm.

the distance between the modified dispersion branches is relatively small. The intersection defines the “resonance frequency”, $k_{\text{res}}L = 3.37$ ($\omega_{\text{res}}/(2\pi) = 6.44 \cdot 10^{14}$ Hz) for $L = 250$ nm, see Fig. 2, that optimizes the considered structure properties for sensor applications. Note that our approach can be also used in the reverse problem - when the design of the multi-layer structure is adjusted to some required operational frequency.

The magnetic field evolution along the x -axis for the solitary metal film SPP modes, i.e., when the buffer and the waveguide thicknesses are zero-valued, $\ell, L \rightarrow 0$, could be derived from Eqs. (1), (2) and (15), where k_x and ω obey Eq. (18). This distribution in (z, x) plane is shown in Fig. 3 for the above “resonance frequency”, ω_{res} .

Field evolution for the eigenmodes of the solitary dielectric waveguide (we consider here the limit or vanishing buffer and the metal layer thicknesses: $d, \ell \rightarrow 0$) could be derived from the same equations but for k_x and ω obeying Eq. (20). The corresponding magnetic field distribution is shown in Fig. 4, for $\omega = \omega_{\text{res}}$.

The magnetic field distributions in the plane (z, x) for three eigenmodes of the multilayer system at the “resonance frequency” are shown in Figs. 5, 6 and 7.

It is seen that by an appropriate fitting of the parameters of a multi-layer structure it is possible to switch between different regimes and to control efficiency of coupling between the waveguide mode and SPP modes.

3. Transmission properties of the multi-layer structure

Consider now transmittance of the described above multi-layer system with the length of the metal layer that differs from the dielectric waveguide length. We calculate here the transmittance as a ratio between the total output energy flux at $x = 100$ μm , and the input energy flux at $x = 0$. The input energy flux at the starting point $x = 0$ corresponds to the solitary waveguide fundamental mode, and the output energy flux is obtained by integrating the x -component of the energy flux density across the section $x = 100$ μm from $z = -3$ μm to $z = 6$ μm . The

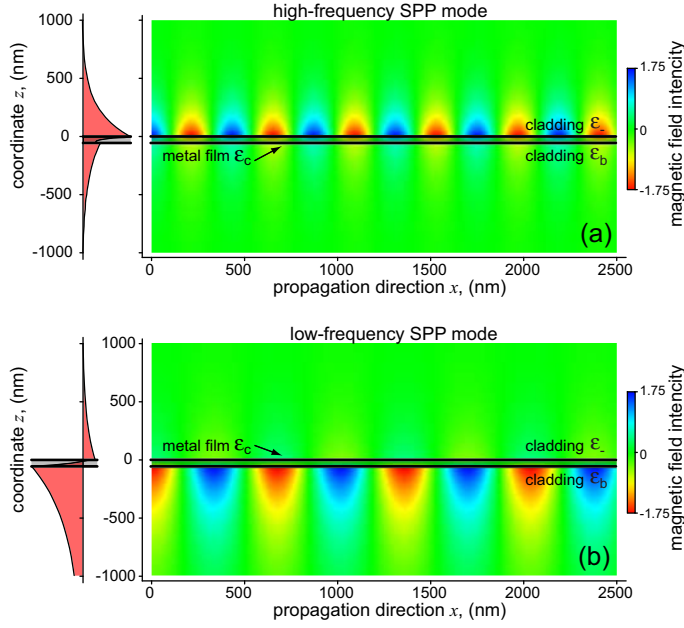


Fig. 3. The magnetic field distribution for the two SPP eigenmodes of the solitary metal film at $\omega = \omega_{\text{res}}$ ($\omega_{\text{res}}L/c = 3.37$). $\alpha_{\text{high}}^2 = 2.268$, $\alpha_{\text{low}}^2 = 2.649$ other parameters are the same as in Fig. 2. The a) (b) figure is the field distribution for the high-frequency (low-frequency) SPP mode of the metal film corresponding to the upper (lower) SPP dispersion curve in Fig. 2.

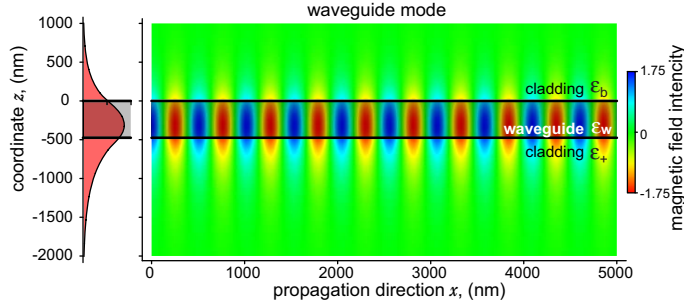


Fig. 4. The magnetic field evolution for the solitary waveguide mode, $\alpha = 1.56$, other parameters are the same as in Fig. 2

electromagnetic field within the structure was obtained by direct numerical simulations of the problem by means of the finite element method (FEM). The calculation length of $100 \mu\text{m}$ was chosen because it was found to be enough to observe the effect. The computation of the longer structures requires significantly larger computer resources. However, it does not add significantly new information — use of a longer computational domain leads to a more precise characterization of a fine structure of the region near the minimum at the resonance frequency (it becomes slightly wider and deeper), but the main features of the frequency dependence of the transmittance are practically not changed.

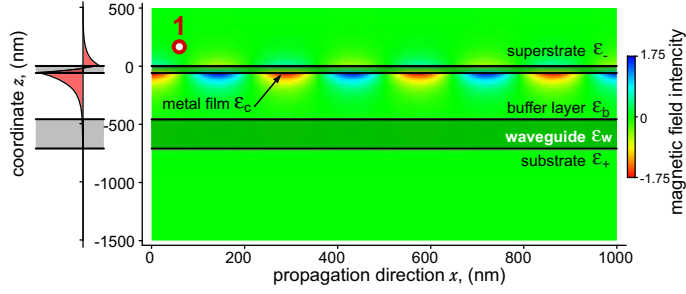


Fig. 5. The magnetic field evolution for the eigenmode of the system corresponding to the point 1 in Fig. 2. Compare the field distribution with that of the right in Fig. 3. The parameters are the same as in Fig. 2.

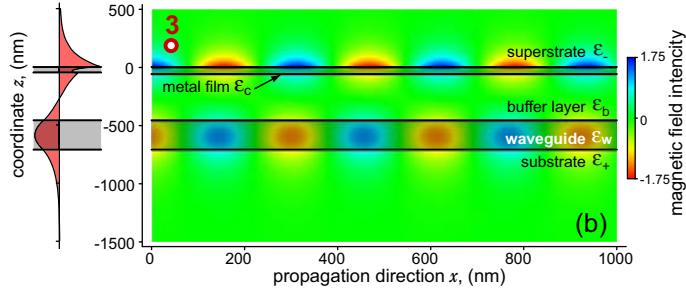
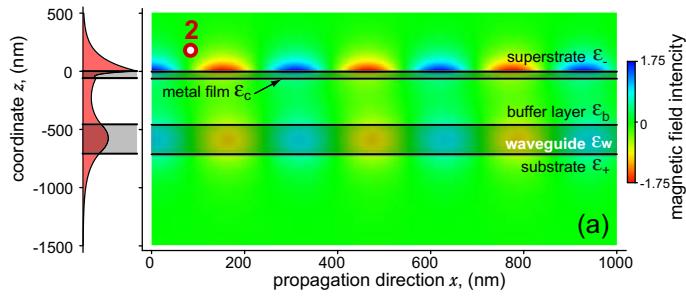


Fig. 6. The magnetic field evolution for the eigenmodes of the system corresponding to the points 2 (a) and 3 (b) in Fig. 2.

The results of the numerical modeling of the transmission coefficient for the long metal film length $\mathcal{L} > 100 \mu\text{m}$ (formally, $\mathcal{L} \rightarrow \infty$) are presented in Fig. 8. The frequency range in the calculations corresponds to the stripe area in the Fig. 2.

One can see rather narrow dip in the transmission coefficient near the defined above “resonance frequency”, shown by the vertical line. Evidently, the transmission falls due to excitation of the SPP modes accompanied by strong enhancement of the dissipative losses. Other local minima of the transmission coefficient are caused by appearance of the radiation losses, cf. Fig. 2. We would like to emphasize that in the considered structure there exists 3 eigenmodes of the system simultaneously (for some given input frequency), see Fig. 2. This fact leads to the field interference pattern easily seen in Fig. 9. For the “resonance frequency” the largest period

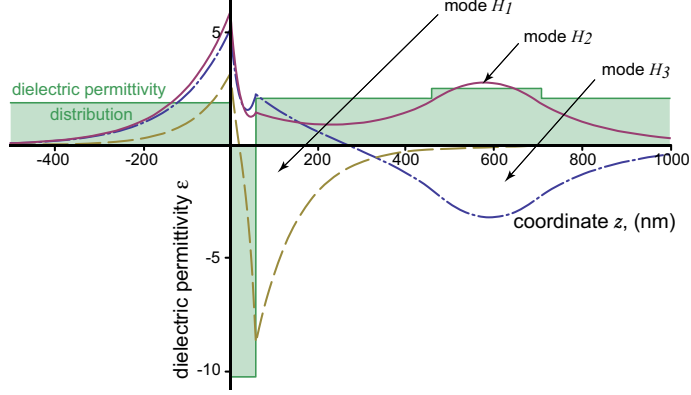


Fig. 7. Squared magnetic field evolution for three eigenmodes of the system for the points 1, 2 and 3 of Fig. 2, and the dielectric permittivity distribution. The parameters are the same as in Fig. 2.

of the pattern is given by the following simple expression:

$$X_{\text{beat}} = \frac{2\pi}{k_{x2} - k_{x3}}, \quad (21)$$

where k_{x2} and k_{x3} are the real parts of the propagation constants of the long-period modes 2 and 3 of the complete system, and could be found from the dispersion relation. In this particular instance $X_{\text{beat}} \approx 69.5 \mu\text{m}$. The small features in the pattern are due to interference of the short-period mode 1 with the long-period modes 2 and 3. That is, corresponding characteristic length of the pattern is $X'_{\text{beat}} \simeq 2\pi/(k_{x1} - k_{x2}) \simeq 3.9 \mu\text{m}$, cf. Fig. 9. These features are in excellent agreement with the results of the recent experimental work [27], where authors consider similar geometry and discuss the coupling length and energy exchange between waveguide and SPP modes.

At the input of the system main part of the energy was in the dielectric waveguide and then is gradually transferred to the metal film. It is seen that the beat half-period $X_{\text{beat}}/2$ gives us a characteristic length for energy exchange between the core- and the high-frequency metal film-localized mode (coupling length) and at the distance $x = X_{\text{beat}}/2$ the maximal transfer of the energy into the metal-film-localized mode occurs, see Fig. 9. Consequently, low transmission coefficients (corresponding to almost total energy transfer from waveguide to the SPP) can be achieved by choosing the metal film length of the order $\mathcal{L}_{\text{opt}} = X_{\text{beat}}/2$, see Fig. 8. This distance is defined as a minimal length of the metal film that can provide for the total energy transfer from the waveguide core to the metal. Since the process of the energy transfer from the core to the SPP and in the backward direction in the absence of losses is cyclic, there exist a number of metal film lengths for which the energy total vanishing in the core appears: $\mathcal{L}_m = X_{\text{beat}}/2 + mX_{\text{beat}}$; $m = 0, 1, 2, \dots$. However, the minimal metal film length has advantage of a large contrast between resonant and non-resonant transmission (transmission at resonant and non-resonant frequencies) due to the small dissipation losses in the shorter metal film. Additionally, the SPP propagation length in our geometry at the resonance frequency is about $100 \mu\text{m}$, that is longer than the minimal length of the metal film. In other words we propose here to make a SPR sensing device, that is shorter (comparable) than SPP propagation length, in contrast to the commonly studied devices with metal film that is much longer than SPP propagation length [10,11,36]. We anticipate that devices with such a minimal length might also

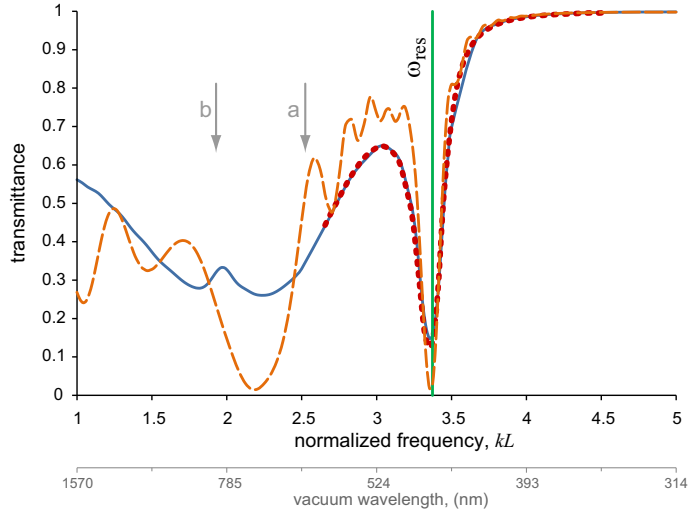


Fig. 8. Frequency dependence of the transmission coefficient for the metal film length $\mathcal{L} > 100 \mu\text{m}$ (solid line), and for $\mathcal{L} = 40 \mu\text{m} \sim X_{\text{beat}}/2$ (dashed line) obtained by direct numeric simulations. The ripples are caused by the finite film length. The arrows a and b indicate the frequency values below which the radiative losses arise for the modes 3 and 2, respectively. Dotted lines present results obtained by the mode expansion procedure. The thickness of the buffer layer is $\ell = 400 \text{ nm}$.

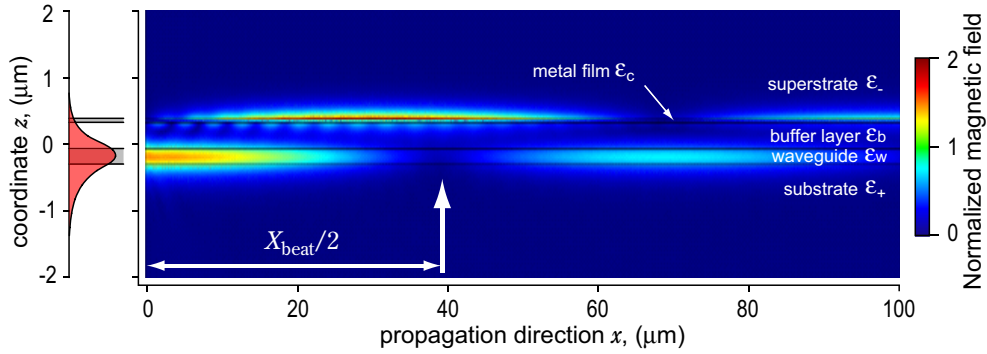


Fig. 9. The squared magnetic field distribution at the resonance frequency, direct numeric simulation.

have enhanced sensitivity. In the recent work [37] it was observed that with decrease in sensing region length, the sensitivity, signal-to-noise ratio are both increasing and the resolution also improves. However, analysis of the sensitivity and signal-to-noise ratio issues for the devices with minimal sensing region length proposed here are beyond the scope of this paper and will be discussed elsewhere.

We stress that it is clearly seen in Fig. 8 that the effect is even more pronounced as compared with the long-film system. Indeed, the transmittance is about zero at the resonance frequency for the dashed curve corresponding to the metal film length of $\mathcal{L} \approx X_{\text{beat}}/2$. This means, in particular, that there is no need to make a millimeter-long [10, 11, 36] film in order to observe

strong transmittance suppression due to the SPR resonance. This feature might be of a particular interest for device miniaturization and integration. The ripples in the frequency dependence of the transmittance coefficient are due to the finite length of the metal film. In Fig. 10 the

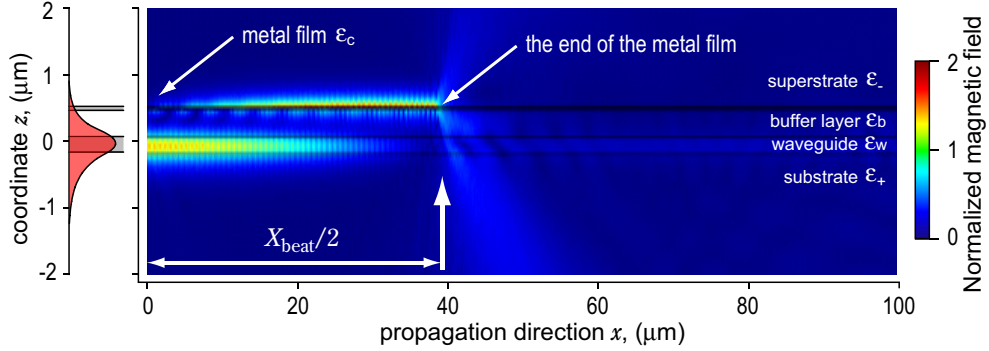


Fig. 10. The squared magnetic field evolution at the resonance frequency for the structure with the metal film, which is cut at some special length of $40 \mu\text{m}$. Direct numeric simulation.

distribution of the squared magnetic field is depicted. It is simulated at the resonance frequency for the system with the metal film of the length $\mathcal{L} = 40 \mu\text{m}$. It is seen that, indeed, near the metal film end the energy flux is concentrated close to the film, demonstrating approximately a total energy transfer from the core into the SPP mode and consecutive scattering out of the system at the metal film edge. As a result, the energy flux in the cross-section $x = 100 \mu\text{m}$ is practically disintegrated.

Finally, we would like to discuss briefly the possibility to apply approximate approach that can be used when a direct numerical modeling becomes time consuming. The fields evolution and transmittance through the structure can be approximately found using the well-known mode expansion method [35]. We would like to point out that there exist rather advanced theoretical methods for analysis of the excitation of surface plasma waves in integrated-optical waveguide structures [36], however, in our geometry it appears to be sufficient to apply a more simple and straightforward mode expansion approach in the following realization. Note that in the considered configurations the homogeneity of the multi-layer structure along the x -axis is preserved (e.g. no gratings are used), there will be no energy transfer (energy exchange) between the eigenmodes of the complete structure during the propagation. Therefore, it is possible to express any arbitrary incoming field distribution — the fundamental waveguide mode of the dielectric waveguide $H_w(x, z, \omega)$ in our example — at the point $x = 0$ in the basis of the eigenmodes of the complete system, $H_i(x, z, \omega)$, see Fig. 7. In other words, we calculate what energy each mode would carry through the structure. Applying this expansion we obtain the field evolution in an arbitrary point x along the structure:

$$H(x, z, \omega) = \sum_i C_i(\omega) \cdot H_i(x, z, \omega),$$

$$C_i(\omega) = \int H_w(0, z, \omega) \frac{k_{xi}(\omega)}{k(\omega)\epsilon(z, \omega)} H_i^*(0, z, \omega) dz, \quad (22)$$

where H_i are the eigenmodes of the complete system, H_w is the input fundamental waveguide mode of the dielectric waveguide, k_{xi} are the wavevectors of the eigenmodes of the complete system. Using Eq. (22) it is easy to calculate the transmittance through the structure, Fig. 8.

The comparison of the direct numeric simulations and the modes expansion method shows an excellent agreement as it can be seen in Fig. 8.

4. Conclusion

We have examined the properties of a multi-layer hybrid device combining the waveguide and surface plasmon polariton modes in a planar geometry. Our main focus here was on the analysis of the feasibility to control mode coupling efficiency through the system design rather than via using additionally written gratings. We have demonstrated that by the proper design of the multi-layer structures it is feasible to achieve substantial reduction in the length of the device.

We have shown that in the considered scheme (without using additional gratings) of the SPR-based sensors there exists an optimal length of the metal film. Such an optimal length is defined by the characteristic (coupling) distance of the energy exchange between the waveguide core and SPP mode. Moreover, there is a set of preferable metal film lengths (sensing region lengths), which are multiples of the coupling distance. The minimal sensing region length offers advantage of higher sensitivity and better signal-to-noise ratio and an improved resolution as it was observed in the recent work [37]. Minimization of the sensing region length also provides a better contrast between resonant and non-resonant transmission (transmission at resonant and non-resonant frequency), due to the small dissipation losses in the shorter metal film. In general, SPR sensor with the minimal metal film length utilizes the effect of SPP-photon transformation rather than SPP dissipation in the metal plate. In other terms our design analysis provide a guidance where to cut a metal film to make a short sensing device. The obtained results might be important for miniaturization and integration of a range of nano-optic systems such as e.g. bio- and chemical sensors, frequency-selective polarizers, and other devices.

We have shown that an appropriate choice of the operational (resonance) frequency could be derived from a rather simple examination of the intersections of the waveguide and SPP dispersion curves resulting in their hybridization. This opens a way of an efficient excitation of the surface plasmon resonance by the waveguide mode and vice versa. In the situations when the required operational frequency (wavelength) is defined by the external conditions our results can be used as the design rules for a specific multi-layer device to operate at the desirable frequency. Evidently, hybridization — coupling of the waveguide and SPP modes occurs not only at a single frequency point, but rather in some spectral interval. Shift of an operational frequency from an optimal value leads to gradual reduction of the efficiency. Our results indicate that a characteristic length of the devices satisfying the resonance conditions (accompanied by a high level of hybridization) required for an efficient energy transfer between waveguide and SPP modes could be as short as tens of micrometers. This is quite an important departure from the characteristic millimeter-scale [10, 11, 36] lengths of conventional devices. Our scheme can be potentially generalized to other geometries, for instance, it can be applied to the cylindrical (fiber) geometry. By an appropriate selection of the parameters the operational (resonance) frequency could be shifted into the near infrared region including telecom windows near 1500 nm. This can be achieved, for instance, by increasing the waveguide layer thickness up to 350 nm and simultaneous decrease of the metal layer thickness down to 30 nm. The minimum transmission of the multi-layer structure considered here depends essentially on the dielectric properties of the media adjacent to the metal film (the superstrate). Therefore, small variations in the refractive index of this medium would result in a strong shift of the transmission dip offering new opportunities and perspectives for the sensor applications.

Acknowledgment

The authors would like to thank Dr. A. Nikitin, Dr. T. Allsop and Dr. S. Derevyanko for helpful discussions. This work was supported by the Royal Society, the European Programme INTAS

(INTAS YS 05-109-5182) and STCU grant No 3979.